



Article

# Analysis, Design, and Experimental Results for a High-Frequency ZVZCS Galvanically Isolated PSFB DC-DC Converter over a Wide Operating Range Using GaN-HEMT

Abdullah Eial Awwad

Department of Electrical Power Engineering and Mechatronics, Faculty of Engineering, Tafila Technical University, Tafila 66110, Jordan; [abdullah.awad@ttu.edu.jo](mailto:abdullah.awad@ttu.edu.jo)

**Abstract:** This paper investigates the potential of the emerging gallium nitride (GaN) high-electron mobility transistors (HEMT) power devices to meet certain power conversion challenges. The advantages of utilizing GaN HEMT transistors in a high-frequency, high-power isolated DC-DC topology are explored experimentally. Using the GaN HEMT's parasitic elements, e.g., output capacitance, and the leakage inductance of the transformer, a soft switching zero-voltage zero-current switching (ZVZCS) phase shift converter is proposed. Accordingly, the freewheeling current is terminated, and soft switching is realized for most of the primary and secondary active devices. Furthermore, without using any additional circuitry, the overshoot voltage across the bridges of active rectifier diodes is clamped at their voltage level. In addition, a high-frequency power transformer is optimized to minimize the overall transformer losses (e.g., winding and core losses). Combined the conductor types, e.g., litz wire and copper foil, shows good electrical and thermal performance by reducing the AC and DC resistance. Finally, a 5 kW, 100–250 kHz prototype is built and tested. The experimental results show a conversion efficiency of up to 98.18% for the whole converter.



**Citation:** Eial Awwad, A. Analysis, Design, and Experimental Results for a High-Frequency ZVZCS Galvanically Isolated PSFB DC-DC Converter over a Wide Operating Range Using GaN-HEMT. *World Electr. Veh. J.* **2022**, *13*, 206. <https://doi.org/10.3390/wevj13110206>

Academic Editors: Diego Bellan and Jelena Loncarski

Received: 26 September 2022

Accepted: 29 October 2022

Published: 2 November 2022

**Publisher's Note:** MDPI stays neutral with regard to jurisdictional claims in published maps and institutional affiliations.



**Copyright:** © 2022 by the author. Licensee MDPI, Basel, Switzerland. This article is an open access article distributed under the terms and conditions of the Creative Commons Attribution (CC BY) license (<https://creativecommons.org/licenses/by/4.0/>).

**Keywords:** GaN HEMT; phase shift full bridge; isolated DC-DC converter; PSFB; high-frequency transformer; zero-voltage zero-current switching; soft switching; wide bandgap (WBG)

## 1. Introduction

Currently, wideband gap (WBG) semiconductors are emerging candidates for high-power applications because of their lower on-state resistance and faster switching frequency, compared to conventional transistors, such as silicon (Si) MOSFETs and IGBTs [1–3]. Due to their superior characteristics, silicon carbide (SiC) and gallium nitride (GaN) high-electron mobility transistors (HEMT) have been the subject of extensive study and development. In terms of their application, the most advantageous features of GaN HEMT devices are their high breakdown field, high thermal conductivity, high-temperature operation, and minor on-state resistance [4–6].

Currently, the use of medium and high-power DC-DC converters is growing rapidly in different applications, including renewable power conversion [7], hybrid electric vehicles [8], power distribution in the micro-grid system [9], and storage systems [10]. The phase-shifted full bridge (PSFB) converter is commonly utilized as a DC-DC stage for high-power applications, and it is a feasible alternative for DC-DC converters.

In electric vehicle (EV) applications, the DC-DC converter is an essential part. Due to the extensive conversion ratio between the input and output, the galvanic isolation with specific turns ratio is preferred. A recent study has summarized the current advancements in GaN WBG semiconductor devices, particularly for EV applications [11]. The study investigates how GaN devices may be used to realize high-efficiency and high-power density converters in EV applications. Reference [12] proposed an integration method of auxiliary power modules and onboard battery chargers, which provide simultaneous operation without an extra circuit and ZVS. This improves the total efficiency, as well as

volume and cost. A previous study investigated a modified multi-port DC-DC converter based on Z-Quasi Resonant for off-board EV battery charging [13]. A control strategy for charging and discharging EV batteries is proposed. Prior work introduced a multiple dual active bridge (DAB) DC-DC stage for EV fast charger. Generalized small-signal modeling and a generalized control approach were proposed to ensure equal power-sharing [14].

The advantages of applying the GaN HEMT devices in the PSFB converter have rarely been discussed in the literature [5,15]. However, the benefit of using SiC MOSFET in the PSFB converter has been introduced [16]. The experimental results for 10 kW, 250 kHz prototypes validate the feasibility of using SiC transistors. Indeed, clamping the overshoot voltage across the rectifier diodes and achieving soft switching in a wide load power range are the main benefits of using SiC MOSFETs in such topology. Using conventional transistors, different studies have focused on improving efficiency and achieving a wide soft switching operating range [17–19]. Other earlier studies have suggested adding snubber circuits and recovery clamp circuits as workable options to suppress the overvoltage across the output rectifier diodes [20–22]. These techniques have a large impact on the clamping of the voltage overshoot over the secondary side but increase the control complexity and add more losses. Furthermore, a previous study [23] used the capacitive output filter to minimize the diode rectifier ringing. This minimization of the diode rectifier ringing allows switching devices to operate at low switching losses under zero-voltage switching (ZVS).

Currently, the HF magnetic components are the bulkiest components of the high-frequency (HF) power converter. In the PSFB topology, the high-frequency transformer (HFT) is a design limitation to achieving high power density [24].

The transformer core and winding wire selection should be optimized for proper design to minimize the core and winding losses. In addition, the selection of the core material is critical in HFT design due to its impact on the cost, efficiency, and volume [3,25,26]. Moreover, the influence of wire types and winding arrangements are critical parameters for enhancing the dynamic performance of the HFT. To minimize winding losses, multi-strand HF litz wire or copper foil are frequently employed. According to previous work [24,27], to reduce the overall winding losses, the ideal number of litz wire strands should be chosen with an AC resistance ( $R_{AC}$ ) that is almost twice as great as its DC resistance ( $R_{DC}$ ). The skin and proximity effects are significantly reduced using litz wire. In contrast, greater thermal resistance is anticipated due to the several isolated strands, making it difficult to cool the litz wire.

Furthermore, the proximity effect is reduced by interleaving the primary and secondary windings, while optimizing the foil thickness effectively reduces the skin effect [24,27]. The copper foil plate is preferred over other materials for usage in high-current applications because of its larger width-to-thickness ratio. Due to this ratio, it offers higher heat conduction, making it possible to accomplish effective heat transmission to the surrounding area.

This work experimentally assesses the advantages of using GaN HEMT devices in the high-frequency, high-power DC-DC converter. First, the dynamic performance of the GaN HEMT is evaluated with different operating conditions. Then, the design optimization of the transformer is presented, and the impacts of different conductor types and winding arrangements are investigated. Finally, a soft switching zero-voltage zero-current switching (ZVZCS) PSFB converter is proposed. The parasitic output capacitance of the GaN HEMT and the power transformer's parasitic leakage inductance are used to achieve soft switching, which results in a low-cost, high-efficiency, lightweight, and compact converter design. A 5 kW, 100–250 kHz prototype experimentally demonstrates an efficiency of up to 98.18% for the full converter.

## 2. PSFB DC-DC Converter

The isolated PSFB DC-DC converter (Figure 1) consists of a controlled GaN HEMT full-bridge inverter at the input (GaN Systems GS66508T), an HF transformer providing

galvanic isolation and voltage level conversion, and a Schottky barrier diode (SBD) bridge rectifier (ROHM SCS230AE2) as the output stage.

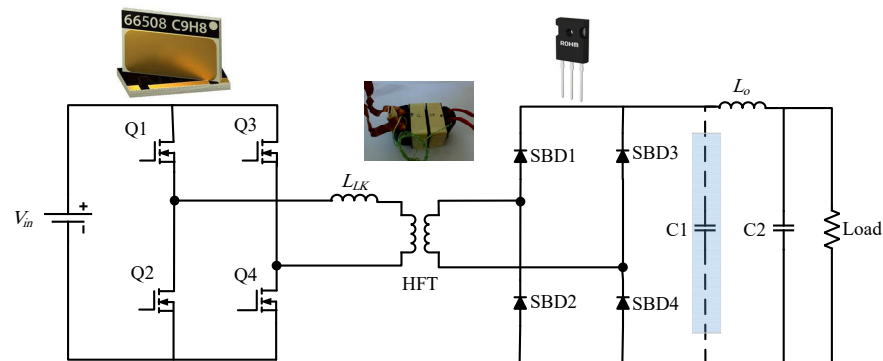


**Figure 1.** Topology of the GaN HEMT PSFB converter.

In this paper, the circuit parasitics, such as the output parasitic capacitance of the GaN devices ( $C_{oss}$ ) and the transformer leakage inductance ( $L_{LK}$ ), are used to achieve ZVZCS. To ensure resonant discharge of the  $C_{oss}$ , the two legs of the controlled GaN HEMT full bridge operate in phase-shift mode. The ZVS of the leading leg (Q1 and Q2) is achieved with help of energy storage in both the transformer leakage inductor and the output filter inductor ( $L_o$ ). The zero-current switching (ZCS) can be achieved for the lagging-leg (Q3 and Q4) during the freewheeling diode transition by forcing the primary current ( $I_p$ ) to zero.

The simulated key waveforms of the ZVZCS PSFB converter are shown in detail in Figure 2. As presented, the lagging leg is turned off with ZCS by forcing the primary current to reduce to zero at  $t_3$ . At this time, Q1 is turned off, and the primary current charges the output capacitance of Q1 ( $C_{oss1}$ ) and discharges the output capacitance of Q2 ( $C_{oss2}$ ). Furthermore, the leading leg always achieves ZVS; indeed, even a minimum primary current amplitude is reached with the help of the energy storage ( $E_L \propto I_p^2$ ).

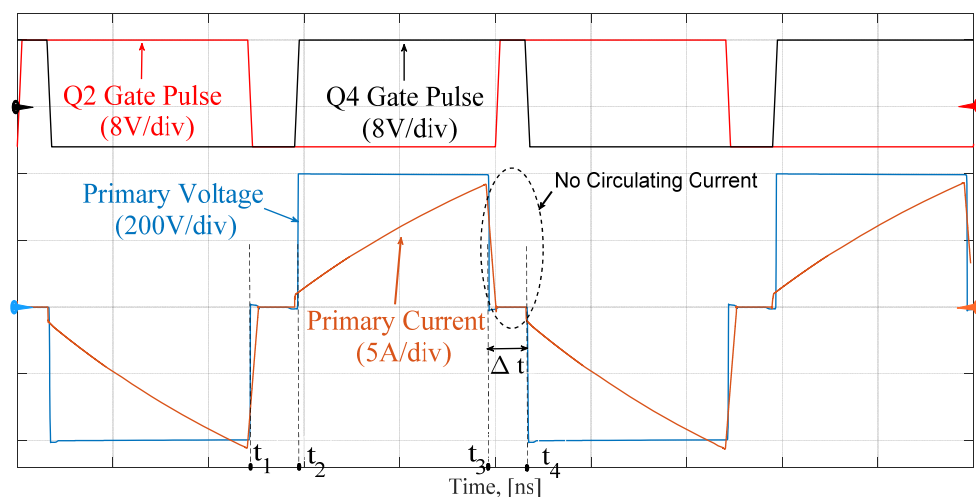


**Figure 2.** Main waveforms of the PSFB converter.

However, one of the main advantages of this topology is that as the primary current reaches zero, no more power is supplied to the load. This phenomenon mainly occurs because the SBD1 and SBD2 become reverse biased, and, hence, the switching losses of the output rectifier diodes and the reverse recovery losses are eliminated. To ensure a continuous current in the load side during the interval ( $\Delta t$ ; Figure 2), the output filter capacitance (C2) is used to supply the load current. In this context, contrary to the Si-based

converter, the circulating current in the primary side is eliminated during the freewheeling period,  $\Delta t$ .

Conversely, the output capacitor (C1) is used to suppress the voltage spikes generated during the power transmission stage that appear across the rectifier bridge.

Moreover, at  $t_4$ , as the primary current is zero, and due to the limitation of the current slope caused by the transformer leakage inductance, the switch Q3 can be turned on with ZVS. Conversely, at  $t_2$ , either ZVS or a hard-switching (HS) state with a relatively small current will cause Q4 to turn on. The switching states of the proposed topology are summarized in Table 1.

**Table 1.** Switching states of the proposed topology.

	Turn on	Turn off	
GaN HEMTBridge	Q1	ZVS	HS with a relatively small turn-off current
	Q2	ZVS	HS with a relatively small turn-off current
	Q3	ZVS or HS with a relatively small turn-on current	ZCS
	Q4	ZVS or HS with a relatively small turn-on current	ZCS

### 3. Design Considerations

#### 3.1. Switching Device Selection

Fast switching is present in GaN HEMT devices, and the process of turning on and off is accompanied by an unwanted current and voltage ringing. Therefore, in order to achieve the optimal utilization of these devices, it is necessary to completely comprehend the switching behavior and, hence, determine the limiting factors in dynamic processes, e.g., turn-on and turn-off transitions.

In this paper, the commercial GaN HEMT transistor (GaN Systems GS66508T) is used as an active device. To characterize the switching performance of the device under test (DUT), the standard double-pulse test (DPT) circuit with inductive load was set up (see Figure 3a).

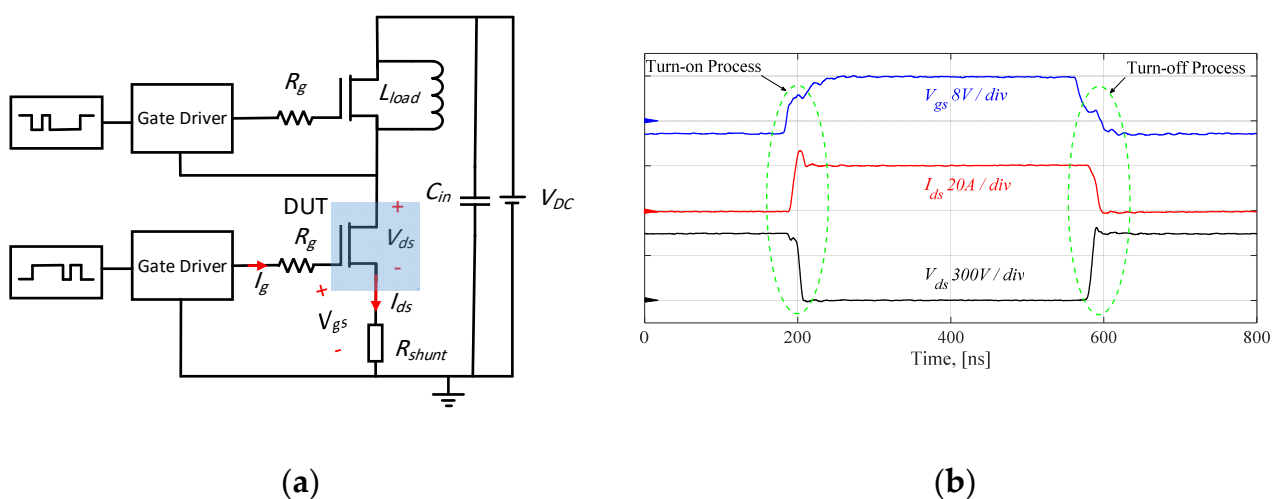


**Figure 3.** Double-pulse test circuit: (a) schematic of the DPT and (b) typical waveforms.

Figure 3b depicts the typical inductive double-pulse switching waveforms, the drain-source voltage ( $V_{ds}$ ), the drain-source current ( $I_{ds}$ ), and the gate-source voltage ( $V_{gs}$ ). As

shown in the figure, at the end of the first pulse and the beginning of the second pulse, the device's switching dynamic waveforms are recorded.

The switching energy loss ( $E_{loss}$ ) is calculated directly from the measurement, according to the following equation:

$$E_{Loss} = \int_t v_{ds}(t) i_{ds}(t) .dt \quad (1)$$

The switching experiments were conducted up to 400 V<sub>DC</sub>, with different case temperatures ( $T_c$ ) and varying load currents from 2 A to 20 A. Figure 4 illustrates the measured turn-on ( $E_{on}$ ) and turn-off ( $E_{off}$ ) switching energy losses at two different case temperatures.

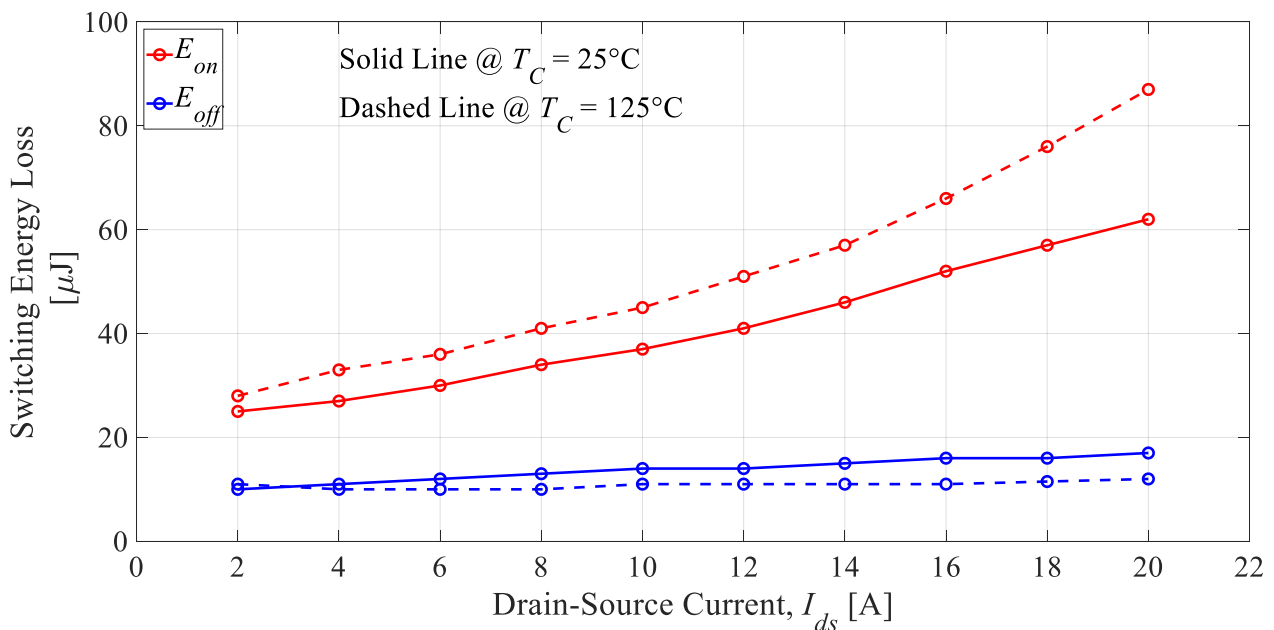


**Figure 4.** Switching energy loss as a function of the drain-source current at 400 V and two different case temperatures.

As expected, with increased current levels, the overall switching losses increase. In detail, as shown in Figure 4, the turn-off loss drops slightly as the temperature increases. This is mainly due to the fact that the plateau voltage increases as the temperature increases. A higher plateau voltage means there is a faster voltage decrease from the plateau to the threshold voltage. A high rate of change of  $v_{ds}$  ( $dv_{ds}/dt$ ) reduces the overlap interval between the channel current and the applied voltage, thus, minimizing the loss interval [28].

Conversely, the turn-on loss is more sensitive to temperature. As observed, at  $I_{ds} = 20$  A, the  $E_{on}$  increases by 40.3% when varying the temperature from 25 °C to 125 °C.

To explain this phenomenon, the transfer characteristic of the DUT was examined with different temperatures. Figure 5 depicts the measured transfer characteristics with different  $T_c$  at a constant  $V_{ds}$  of 9 V. As shown, in the saturation region, the current is reduced accordingly with the increase in temperature, resulting in a reduction in the average transconductance ( $g_m$ ; Figure 6). As observed, the transconductance decreases by 59% when increasing the temperature from 25 °C to 125 °C. The decrease in  $g_m$  is mainly due to the decrease in both the electron mobility and the electron velocity, and thus limits the displacement current, which results in an increase in the turn-on switching time, and hence the loss [28].

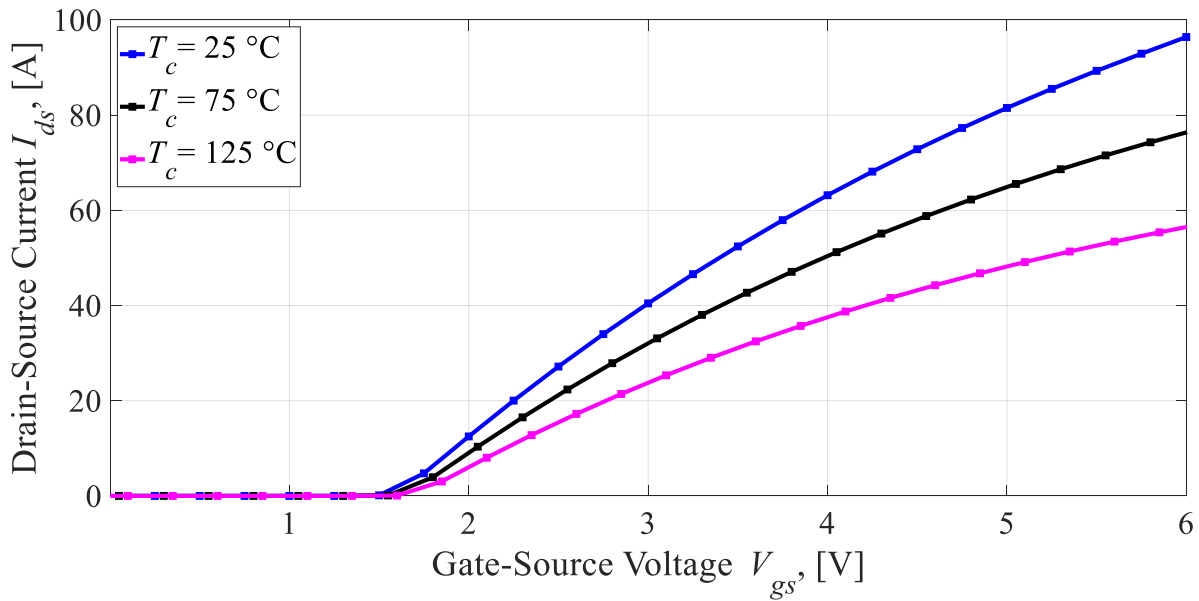


Figure 5. Transfer characteristics measured at different case temperatures.

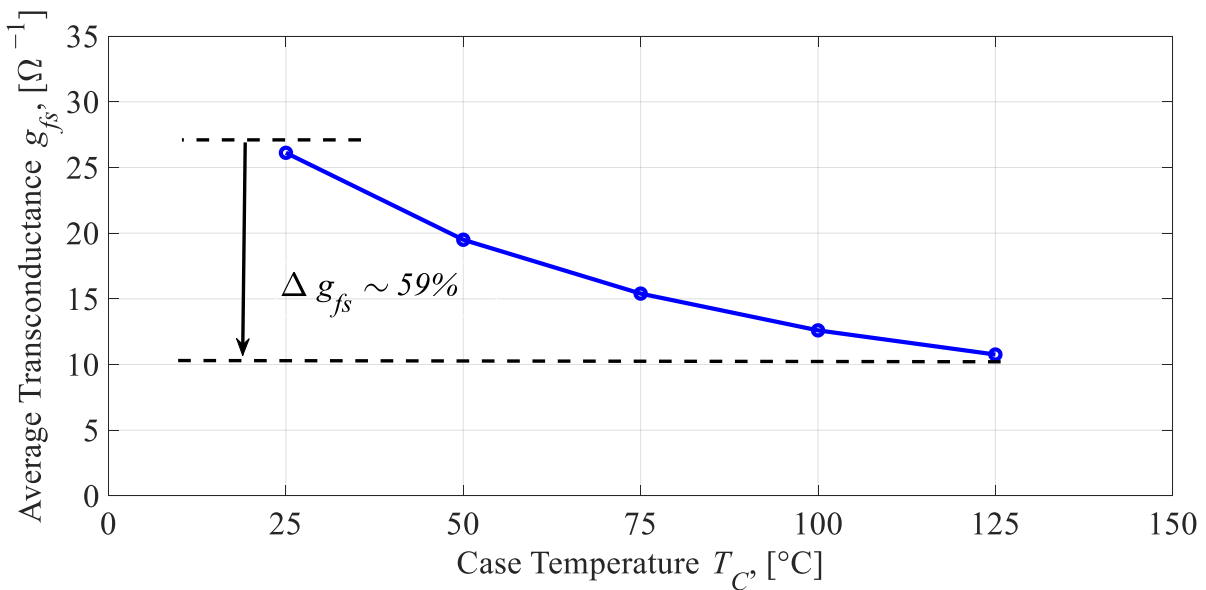


Figure 6. Transconductance as a function of case temperature.

### 3.2. Switching Frequency and Thermal Limitation

As previously mentioned, GaN HEMT devices operate under high temperatures and HF conditions, thus, reducing the overall size and cost of the passive components and resulting in an increase in total power density. Conversely, the thermal design becomes more difficult, necessitating the use of a sophisticated cooling system. Indeed, the cooling system represents a key factor limiting the utilization of the potential advantages of GaN HEMT transistors in high-power converter applications.

In this context, the switching frequency and thermal limitation factors are elucidated to design a high switching frequency power converter that operates continuously with 5 kW output power.

The maximum power dissipated ( $P_{DMAX}$ ) in the high-power semiconductors is calculated as follows:

$$P_{DMAX} = \frac{T_j - T_c}{R_{th}} \tag{2}$$

$$R_{th} = R_{th-jc} + R_{th-ca} \quad (3)$$

where  $T_j$  is the junction temperature,  $R_{th}$  is the total thermal resistance,  $R_{th-jc}$  ( $=0.5 \text{ }^\circ\text{C/W}$ ) is the thermal resistance from the junction to the case, and  $R_{th-ca}$  ( $=0.2 \text{ }^\circ\text{C/W}$ ) is the thermal resistance from the case to the ambient temperature.

The junction temperature is a function of the total power losses and total thermal resistance:

$$T_j = T_c + R_{th}P_{Loss}(T_j) \quad (4)$$

$$P_{Loss}(T_j) = P_{cond}(T_j) + P_{sw}(T_j) \quad (5)$$

where the  $P_{cond}(T_j)$  and  $P_{sw}(T_j)$ , respectively, are the conduction and switching losses as a function of the junction temperature, which is given as follows:

$$P_{cond}(T_j) = D[1 + \alpha_1(T_j - T_o)]R_{on1}I_{ds-RMS}^2 \quad (6)$$

$$P_{sw}(T_j) = [E_{on}(V_{ds}, I_{ds}, T_j) + E_{off}(V_{ds}, I_{ds}, T_j)]f_{sw} \quad (7)$$

where  $R_{on1}$  is the on-state resistance at room temperature ( $T_o$ ) (e.g., for the GS66508T device, the measured  $R_{on1} = 55 \text{ m}\Omega$ ),  $\alpha_1$  is the on-state resistance coefficient ( $\alpha_1 = 0.64 \text{ m}\Omega/^\circ\text{C}$ ),  $I_{ds-RMS}$  is the drain-source RMS current calculated over the on-time duty cycle,  $D$ , and  $f_{sw}$  is the switching frequency.

The maximum power dissipated in the DUT is calculated using Equation (2). The converter is forced-air cooled, giving an estimated case temperature of  $70 \text{ }^\circ\text{C}$  for a power dissipation of  $114 \text{ W}$ . To ensure safe operation, a safety margin ( $\beta$ ) of 20% is assumed.

Therefore, the relationship between the maximum allowable switching frequency and the total losses should satisfy the following constraint:

$$P_{Loss}(T_j) \leq (100\% - \beta)P_{DMAX} \quad (8)$$

$P_{Loss}(T_j)$  can be rewritten as follows:

$$P_{Loss}(T_j) = P_{cond} + f_{sw}(E_{on} + E_{off}) \quad (9)$$

Therefore, the maximum permitted switching frequency ( $f_{sw-MAX}$ ) can be calculated as follows:

$$f_{sw-MAX} = \frac{(100\% - \beta)P_{DMAX} - P_{cond}}{P_{sw}} \quad (10)$$

As a result, the relationship between the maximum permitted switching frequency and the possible output power can be simply calculated. In this work, to prevent overheating of the core and windings and to ensure the safe operation of the GaN HEMT and diode bridges under the use of the forced-air cooling system, the switching frequency was limited to  $250 \text{ kHz}$ .

### 3.3. Design and Optimization of the HF Transformer

The transformer provides galvanic isolation and the required voltage matching in isolated DC-DC converters. In this work, in order to minimize the core and winding losses, the selection of the transformer core and winding wire was optimized. Table 2 shows the operating conditions of the HF transformer.

**Table 2.** DC-DC converter design parameters.

Output Power, $P_{out}$	5 kW
Input Voltage, $V_{in}$	400 V
Output Voltage, $V_{out}$	500–600 V

**Table 2.** Cont.

Switching Frequency, $f_{sw}$		100–250 kHz
Turns Ratio, $n$		1:1.5
Deadtime ( $t_{dead}$ )		70 ns
GaN HEMTs	GS66508T	– Drain-Source Blocking Voltage ( $BV_{DS}$ ) = 650V – On-state resistance ( $R_{on1}$ ) = 55/118 m $\Omega$ (Measured at 25/125 °C).
Rectifier Diodes	SCS230AE2	– Reverse Voltage ( $VR$ ) = 650 V – Continuous Forward Current ( $IF$ ) = 30 A
<b>High-Frequency Transformer</b>		
Ferrite Material		N87
Leakage Inductance, $L_{LK}$		1.9 $\mu$ H
Primary Turns, $np$		10
Primary Windings		4 Litz wires (parallel 100 $\times$ $\varnothing$ 0.05 mm)
Secondary Turns, $ns$		15
Secondary Windings		Copper Foil (36 mm $\times$ 0.15 mm)
DC Resistance, $R_{DC}$		17 m $\Omega$
AC Resistance, $R_{AC}$ , 100/250 kHz		57/71 m $\Omega$

The design methodology proposed in this paper is devoted to minimizing the total power loss, including the core ( $P_{core}$ ) and winding ( $P_w$ ) losses, and hence improving the overall converter performance.

The core loss can be expressed as follows [24]:

$$P_{core} = K f_{sw}^{\alpha} \Delta B^{\beta} A_c l_m \quad (11)$$

where  $K$  is the core loss coefficient,  $\Delta B$  is the peak AC flux density,  $A_c$  is the core cross-section area,  $l_m$  is the core mean magnetic path length, and  $\alpha$  and  $\beta$  are the core loss exponents.

In terms of the winding losses, the following expression can be used [24]:

$$P_w = K_r \frac{\lambda^2 \rho (MLT)}{4 A_{win} k_u A_c^2} \left( \frac{1}{\Delta B} \right)^2 I_{RMS}^2 \quad (12)$$

where  $K_r$  is the normalized value of the AC resistance at HF,  $\lambda$  is the applied primary volt-sec,  $\rho$  is the resistivity of copper,  $MLT$  is the mean length per turn,  $k_u$  is the fill factor,  $A_{win}$  and  $A_c$  are the window and cross-section areas of the core, respectively, and  $I_{RMS}$  is the RMS winding current.

Furthermore, the flux density and the number of turns are considered key parameters in the transformer design. The optimal flux density ( $B_{optimal}$ ) occurs when the first derivative of the total loss ( $P_{tot}$ ) is zero [24]:

$$\frac{dP_{tot}}{d(\Delta B)} = \frac{dP_{core}}{d(\Delta B)} + \frac{dP_w}{d(\Delta B)} = 0 \quad (13)$$

Therefore, the minimum loss can be achieved (Figure 7) if the core operating is designed at the optimal flux density  $B_{optimal}$  [24]:

$$\Delta B_{optimal} = \left( \frac{K_r I_{rms}^2 \rho \lambda^2 M L T}{4 K_u A_{win} A_c^3 l_m f_{sw}^\alpha} \right)^{\frac{1}{\beta+2}} \quad (14)$$

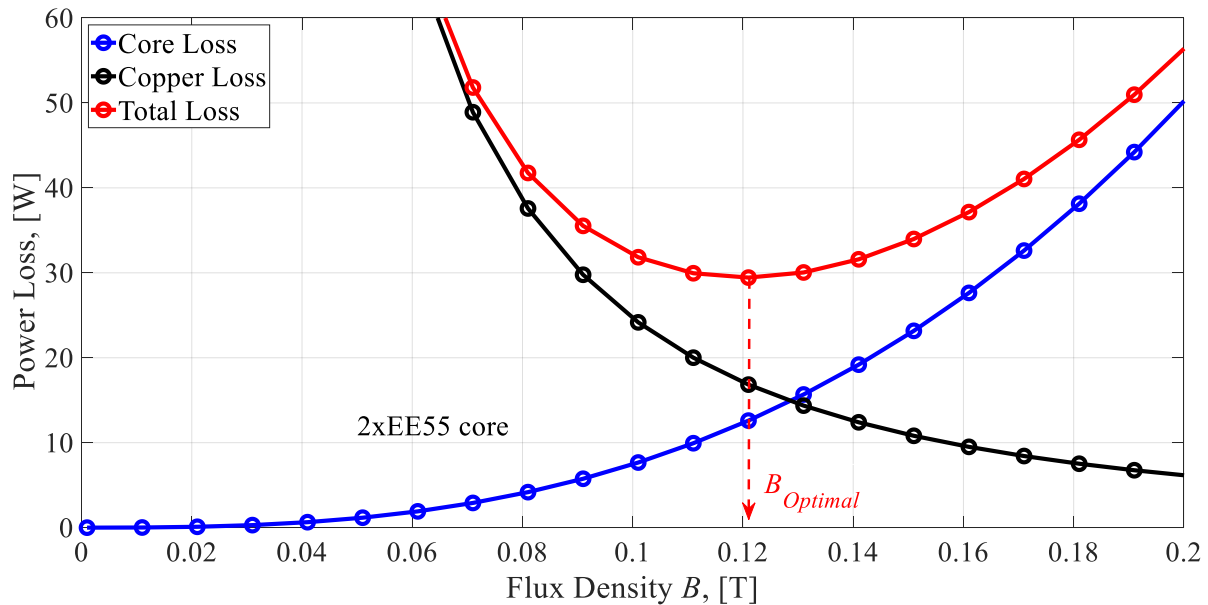


**Figure 7.** The optimal flux density versus the total power loss of the high-frequency transformer.

Moreover, by solving  $\left(\frac{dP_{tot}}{dn} = 0\right)$ , the optimal number of turns ( $n_{optimal}$ ) that minimize the total transformer power loss can be determined:

$$n_{optimal} = \left( \frac{\beta K_r f_{sw}^{(\alpha-\beta)} \left(\frac{V_{in}}{2A_c}\right)^\beta A_c l_m k_u A_{win}}{2\rho K_r M L T I_{rms}^2} \right)^{\frac{1}{\beta+2}} \quad (15)$$

In this work, to avoid the expected high surface temperature rise, a double EE55/28/21 core using N87 material was used in the design. As shown in Figure 7, using Equation (14), the optimal flux density can be calculated as 121 mT and the optimal number of turns as 10. This results in 17 W of winding losses and 15 W of core losses at an  $f_{sw}$  of 100 kHz.

The copper foil plate is chosen over other materials for usage in high-current applications because of its larger width-to-thickness ratio, which means better heat transfer to the ambient temperature can be obtained. In addition, selecting the optimal foil thickness directly reduces the skin effect, and applying the interleaving method to the primary and secondary windings minimizes the proximity effect.

Conversely, using litz wires effectively reduces the skin and proximity effects, but a large core window area is required. Further to this, higher thermal resistance is expected because of the multi-isolated strands, and thus the cooling system becomes inactive.

According to previous work [3,27], combining different conductor types (litz wire and copper foil; Figure 8) provides good electrical and thermal characteristics. With this approach (Table 1), the copper foil is applied to the low-voltage, high-current side, with a cross-section area of 5.4 mm<sup>2</sup> (width: 36 mm × thickness: 0.15 mm). In contrast, the litz wire is applied to the high-voltage side with four parallel 100 strands with a diameter of 0.05 mm.

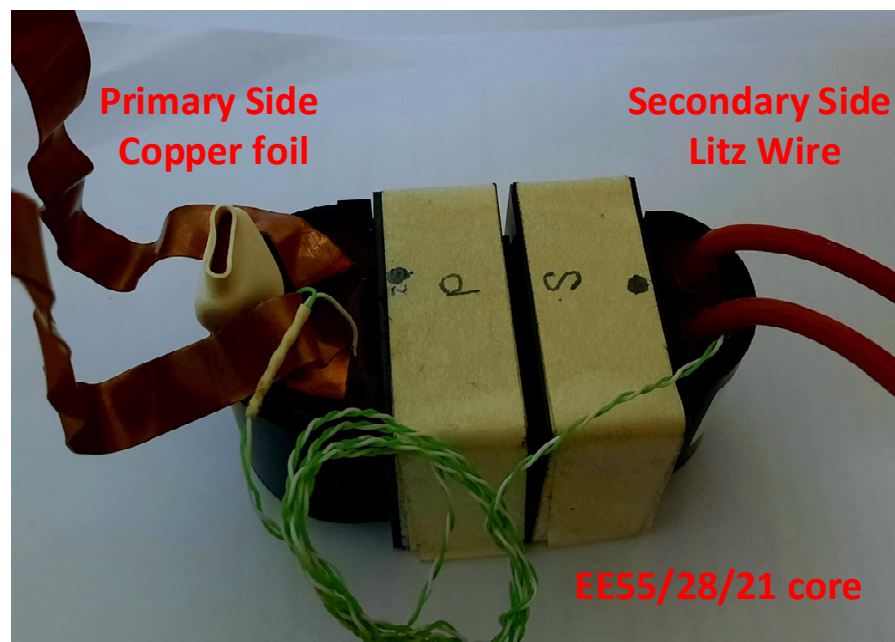


**Figure 8.** The 5 kW ferrite core (N87) high-frequency transformer prototype.

#### 4. Experimental Results and Discussion

In this study, a prototype of a 5 kW ZVZCS PSFB DC-DC converter has been built and tested. A switching frequency in the range of 100–250 kHz is applied. Operating at different switching frequencies provides a clear picture of the optimum efficiency and power density design. Additionally, to drive and control the high-speed power devices, a microcontroller from STMicroelectronics based on the ARM Cortex architecture (STM32F429, clock rate up to 180 MHz) is used.

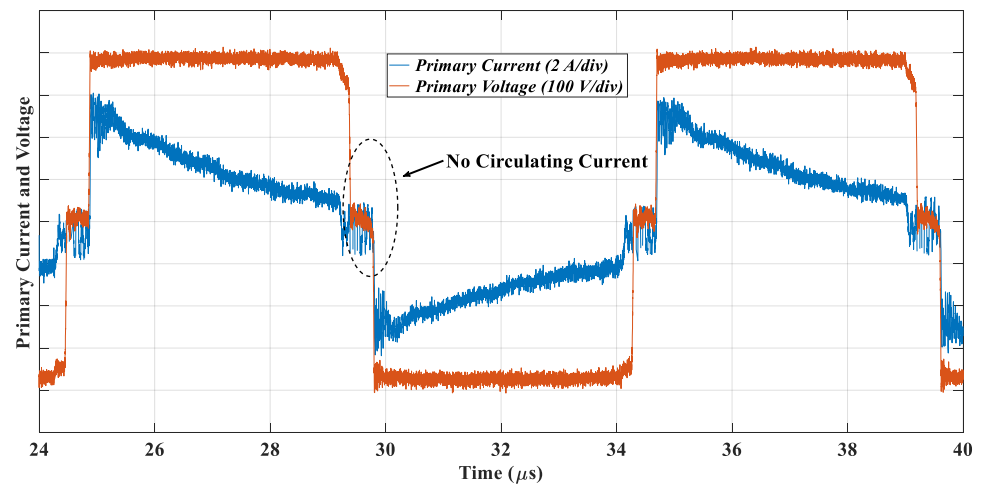
The converter specifications used in this work are shown in Table 1. The key waveforms of the proposed ZVZCS converter at different loads with a switching frequency of 100 kHz are illustrated in Figure 9.

It is clear that the proposed converter is able to operate with ZVZCS even at light load, without any additional auxiliary circuit. As shown, the freewheeling current mode is removed, increasing the overall efficiency. Furthermore, the capacitive output filter clamped the overshoot in the primary and secondary voltages to the appropriate voltage level, eliminating the need for an additional circuit.

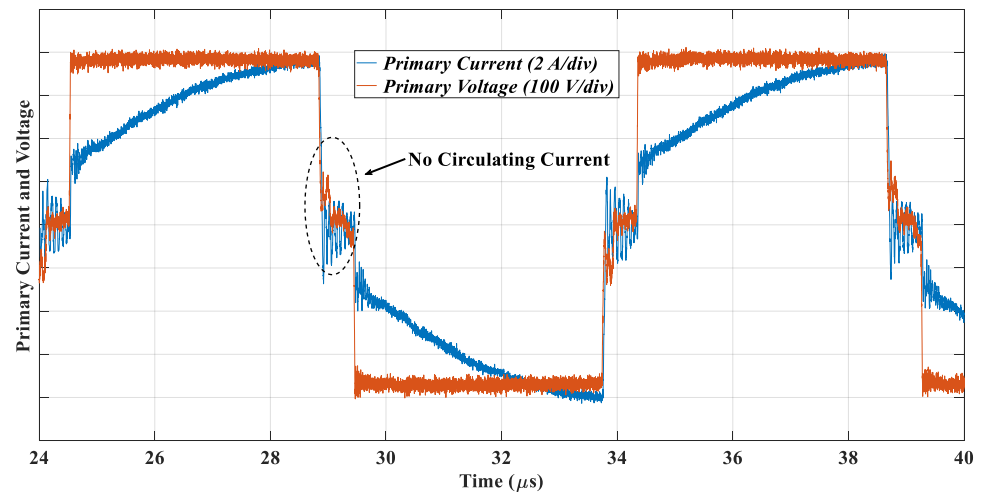
Additionally, the proposed converter was investigated at a higher switching frequency. Figure 10 illustrates the key waveforms of the proposed ZVZCS at different loads and a fixed switching frequency of 250 kHz.

It can be concluded that, even at a higher switching frequency, the ZVZCS can be achieved using only the small parasitic leakage inductance of the HFT. This achievement of ZVZCS leads to improvements in overall efficiency for a wide power range.

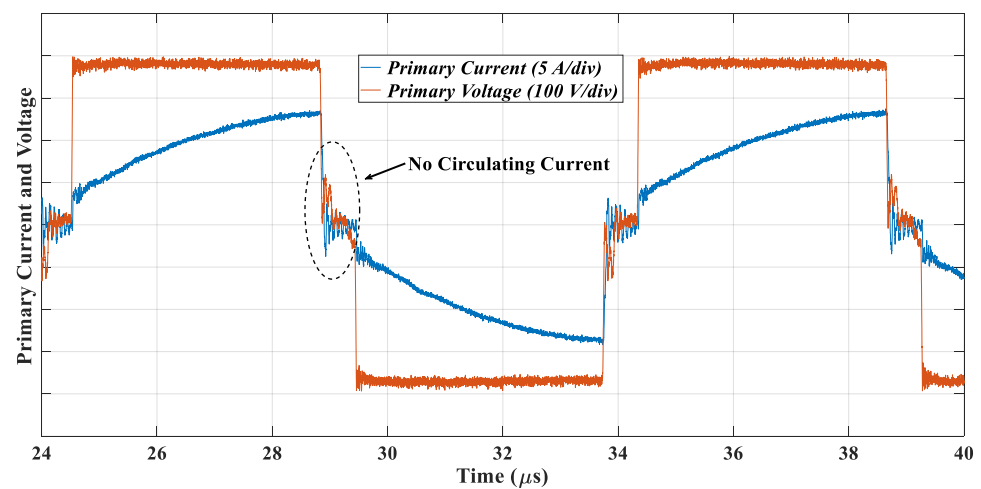
The measured efficiencies of the overall proposed converter at 100 kHz, 150 kHz, and 250 kHz are compared in Figure 11. The design and optimization methodology of HFT, the application of ZVZCS, the optimization of the conductor types (e.g., mixing the litz wire and copper foil), and the superior features of the GaN HEMT devices lead to an efficiency of up to 98.18% for the whole converter.



(a)

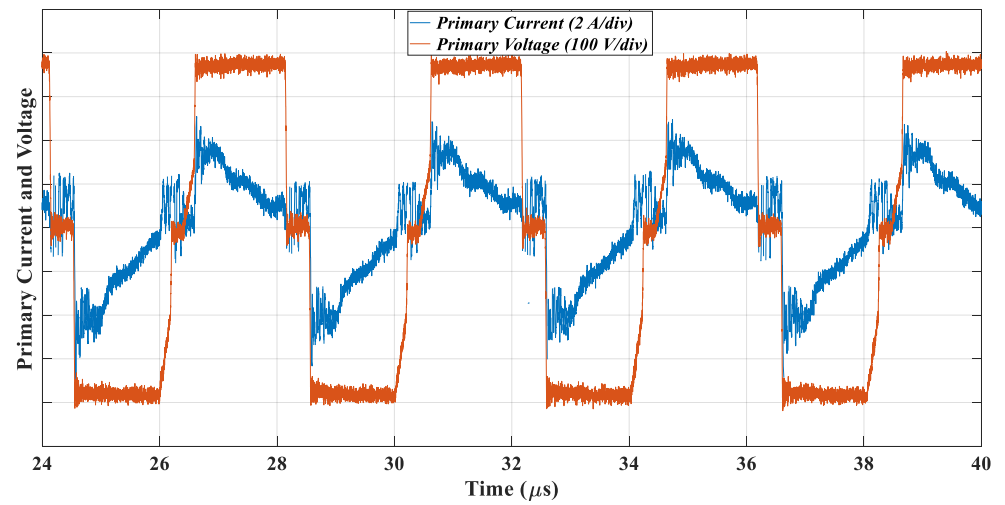


(b)

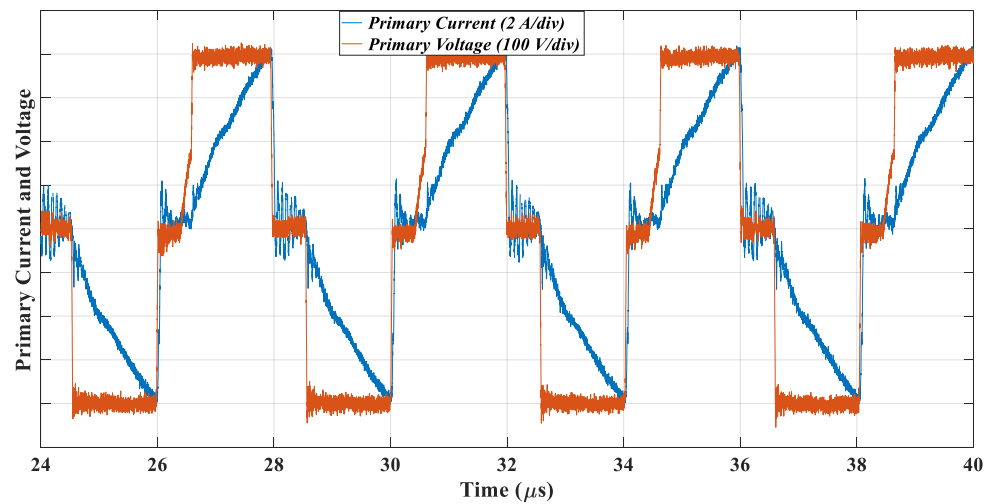


(c)

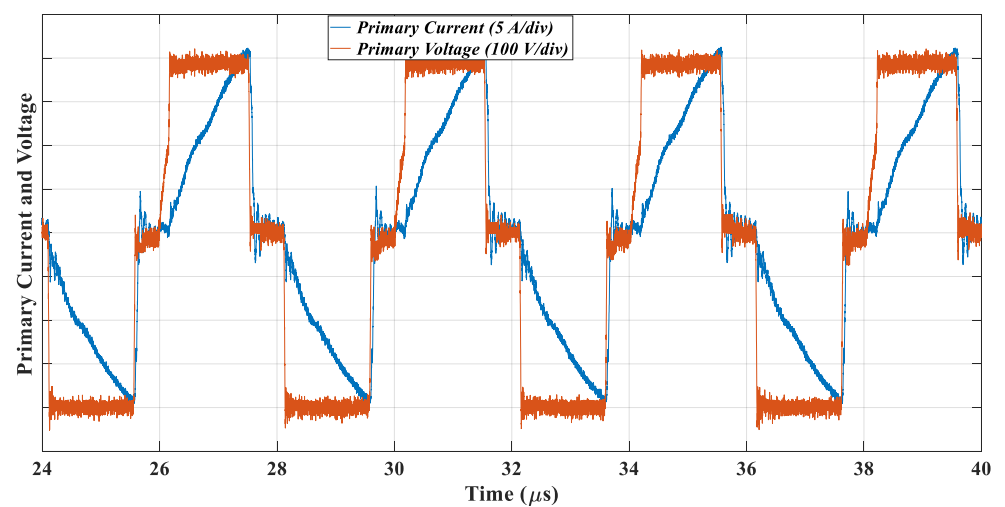
**Figure 9.** Measured operation waveforms at 100 kHz and output powers of (a) 800 W, (b) 3 kW, and (c) 5 kW.



(a)



(b)



(c)

**Figure 10.** Measured operation waveforms at 250 kHz and output powers of (a) 800 W, (b) 3 kW, and (c) 5 kW.

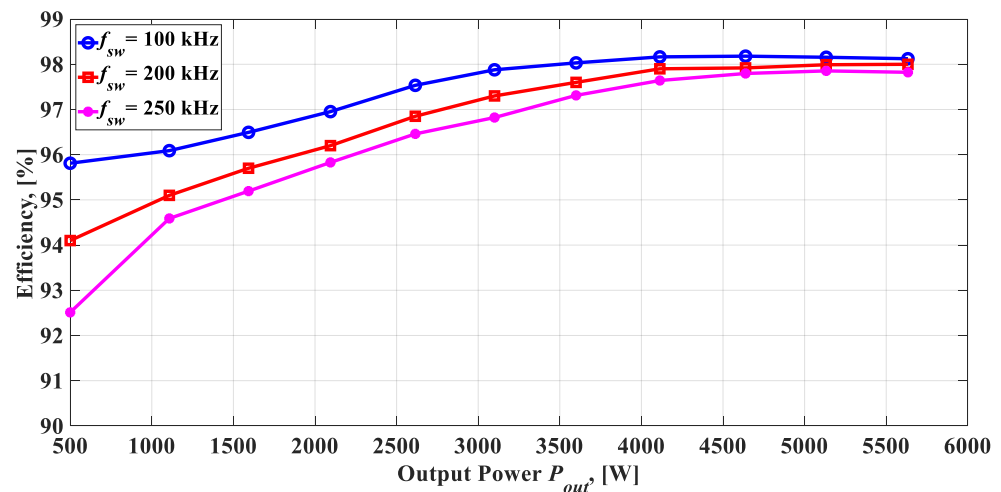


**Figure 11.** Efficiency comparison of the whole proposed converter at different switching frequencies.

The measured power losses are separated into GaN HEMT power loss (e.g., conduction and switching) and other losses (e.g., core and winding losses of the HFT, rectifier diodes, filter, DC-link, etc.; Figure 12). To extract the power losses, the input and output power are measured using a power analyzer (Zimmer LMG671). The high-speed current and voltage switching of the GaN HEMT and HFT are captured with high-bandwidth meters of 200–2000 MHz. Furthermore, the total equivalent series resistance (ESR) of the HFT is measured as a function of frequency. Specifically, the switching losses of the GaN HEMT devices at given turn-on and turn-off currents are extracted based on the measured DPT results shown in Figure 4. The conduction loss is estimated using the measured on-state resistance. Finally, the core and winding losses are calculated based on Equations (11) and (12), respectively.

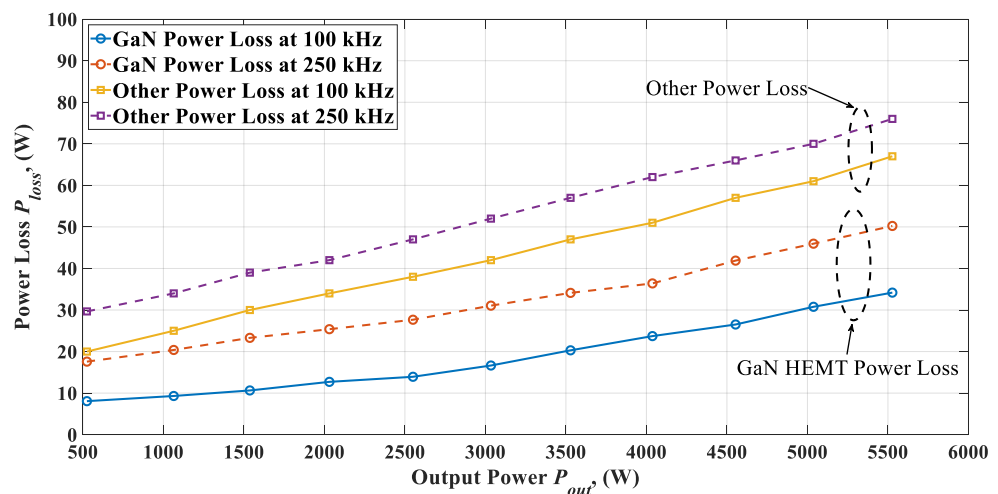


**Figure 12.** Loss distribution of the proposed converter at different output powers and two different switching frequencies.

Additionally, for the other losses, e.g., conduction and switching losses of leading and lagging legs, the losses of the output rectifier diodes, the loss breakdown methodology described in [16] is adaptive and applied in this work.

As an example, Figure 13 shows the loss distribution at 5 kW and different switching frequencies. As demonstrated, at  $f_{sw} = 100$  kHz, the full bridge GaN HEMT loss is about 32% of the overall power losses (23% conduction loss and 9% switching loss of the overall power losses). It is worth mentioning that even working at high switching frequency

( $f_{sw} = 250$  kHz), the GaN HEMT devices still operate with 40% of the maximum power dissipated (Figure 13).

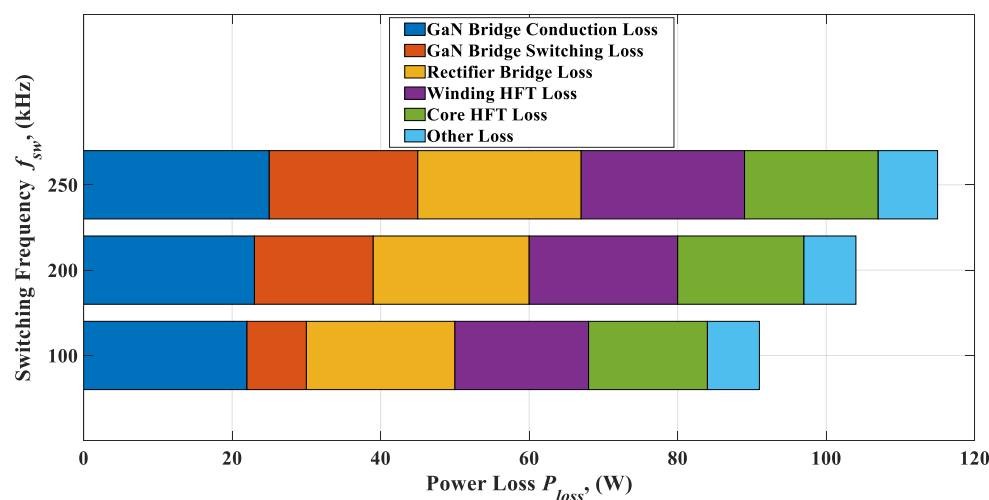


**Figure 13.** Detailed loss distribution of the proposed converter at 5 kW and different switching frequencies.

## 5. Conclusions

In this paper, a design methodology for achieving a soft switching phase shift full bridge converter using GaN HEMT devices is presented. Using the parasitics capacitance of the GaN HEMT, a soft switching ZVZCS PSFB converter is proposed using the power transformer's parasitic leakage inductance.

The main benefits of using the GaN HEMT device in such topology are the elimination of the freewheeling circulating current, the clamping of the overshoot voltage across the primary and secondary bridges, and the obtaining of soft switching in a wide load power range without using additional auxiliary circuits or an additional high-frequency inductor. Furthermore, in this study, the design and optimization of a high-frequency, high-power transformer are presented. In this context, using different conductor types (litz wire and copper foil) shows good thermal and electrical properties.

A 100–250 kHz, 400/600 V, 5 kW GaN-based PSFB prototype was built and tested, which showed a good dynamic performance in the wide load power range and an efficiency of up to 98.18% for the whole converter.

**Funding:** This research received no external funding.

**Data Availability Statement:** Not applicable.

**Conflicts of Interest:** The authors declare no conflict of interest.

## References

- Kimoto, T.; Cooper, J.A. *Fundamentals of Silicon Carbide Technology: Growth, Characterization, Devices and Applications*; Wiley: Singapore, 2014; ISBN 1118313550.
- Suganuma, K. *Wide Bandgap Power Semiconductor Packaging: Materials, Components, and Reliability*; Woodhead Publishing: Oxford, UK, 2018; ISBN 9780081020944.
- Eial Awwad, A. *On the Perspectives of SiC MOSFETs in High-Frequency and High-Power Isolated DC/DC Converters*; Universitätsverlag der TU Berlin: Berlin, Germany, 2020; ISBN 3798330964.
- Morya, A.K.; Gardner, M.C.; Anvari, B.; Liu, L.; Yepes, A.G.; Doval-Gandoy, J.; Toliyat, H.A. Wide Bandgap Devices in AC Electric Drives: Opportunities and Challenges. *IEEE Trans. Transp. Electrific.* **2019**, *5*, 3–20. [\[CrossRef\]](#)
- Ma, C.-T.; Gu, Z.-H. Review of GaN HEMT Applications in Power Converters over 500 W. *Electronics* **2019**, *8*, 1401. [\[CrossRef\]](#)
- Bu, H.; Cho, Y. GaN-based Matrix Converter Design with Output Filters for Motor Friendly Drive System. *Energies* **2020**, *13*, 971. [\[CrossRef\]](#)
- Eial Awwad, A. Dynamic Performance Enhancement of a Direct-Driven PMSG-Based Wind Turbine Using a 12-Sectors DTC. *WEVJ* **2022**, *13*, 123. [\[CrossRef\]](#)

8. Janabi, A.; Wang, B. Switched-Capacitor Voltage Boost Converter for Electric and Hybrid Electric Vehicle Drives. *IEEE Trans. Power Electron.* **2020**, *35*, 5615–5624. [[CrossRef](#)]
9. Shamsi, P.; Fahimi, B. Stability Assessment of a DC Distribution Network in a Hybrid Micro-Grid Application. *IEEE Trans. Smart Grid* **2014**, *5*, 2527–2534. [[CrossRef](#)]
10. Avila, A.; Lucu, M.; Garcia-Bediaga, A.; Iburguren, U.; Gandiaga, I.; Rujas, A. Hybrid Energy Storage System Based on Li-Ion and Li-S Battery Modules and GaN-Based DC-DC Converter. *IEEE Access.* **2021**, *9*, 132342–132353. [[CrossRef](#)]
11. Yadlapalli, R.T.; Kotapati, A.; Kandipati, R.; Balusu, S.R.; Koritala, C.S. Advancements in energy efficient GaN power devices and power modules for electric vehicle applications: A review. *Int. J. Energy Res.* **2021**, *45*, 12638–12664. [[CrossRef](#)]
12. Yu, G.; Choi, S. An Effective Integration of APM and OBC With Simultaneous Operation and Entire ZVS Range for Electric Vehicle. *IEEE Trans. Power Electron.* **2021**, *36*, 10343–10354. [[CrossRef](#)]
13. Harini, S.; Chellammal, N.; Chokkalingam, B.; Mihet-Popa, L. A Novel High Gain Dual Input Single Output Z-Quasi Resonant (ZQR) DC/DC Converter for Off-Board EV Charging. *IEEE Access.* **2022**, *10*, 83350–83367. [[CrossRef](#)]
14. ElMenshawhy, M.; Massoud, A. Modular Isolated DC-DC Converters for Ultra-Fast EV Chargers: A Generalized Modeling and Control Approach. *Energies* **2020**, *13*, 2540. [[CrossRef](#)]
15. Joo, D.-M.; Lee, B.-K.; Kim, D.-S.; Kim, J.-S.; Kim, H.-J. Analysis of GaN HEMT-based phase shifted full bridge dc-dc converter. In Proceedings of the 2015 IEEE International Telecommunications Energy Conference (INTELEC), Osaka, Japan, 18–22 October 2015; pp. 1–5. [[CrossRef](#)]
16. Awwad, A.E.; Badawi, N.; Dieckerhoff, S. Efficiency analysis of a high frequency PS-ZVS isolated unidirectional full-bridge DC-DC converter based on SiC MOSFETs. In Proceedings of the 2016 18th European Conference on Power Electronics and Applications (EPE'16 ECCE Europe), Karlsruhe, Germany, 5–9 September 2016; pp. 1–10. [[CrossRef](#)]
17. Kim, Y.-D.; Cho, K.-M.; Kim, D.-Y.; Moon, G.-W. Wide-Range ZVS Phase-Shift Full-Bridge Converter with Reduced Conduction Loss Caused by Circulating Current. *IEEE Trans. Power Electron.* **2013**, *28*, 3308–3316. [[CrossRef](#)]
18. Ruan, X.; Yan, Y. A novel zero-voltage and zero-current-switching PWM full-bridge converter using two diodes in series with the lagging leg. *IEEE Trans. Ind. Electron.* **2001**, *48*, 777–785. [[CrossRef](#)]
19. Shi, K.; Zhang, D.; Zhou, Z.; Zhang, M.; Gu, Y. A Novel Phase-Shift Dual Full-Bridge Converter with Full Soft-Switching Range and Wide Conversion Range. *IEEE Trans. Power Electron.* **2016**, *31*, 7747–7760. [[CrossRef](#)]
20. Ilic, M.; Maksimovic, D. Phase-Shifted Full Bridge DC-DC Converter with Energy Recovery Clamp and Reduced Circulating Current. In Proceedings of the APEC 07-Twenty-Second Annual IEEE Applied Power Electronics Conference and Exposition, Anaheim, CA, USA, 25 February–1 March 2007; pp. 969–975. [[CrossRef](#)]
21. Mweene, L.H.; Wright, C.A.; Schlecht, M.F. A 1 kW 500 kHz front-end converter for a distributed power supply system. *IEEE Trans. Power Electron.* **1991**, *6*, 398–407. [[CrossRef](#)]
22. Cho, J.-G.; Baek, J.-W.; Jeong, C.-Y.; Yoo, D.-W.; Joe, K.-Y. Novel zero-voltage and zero-current-switching full bridge PWM converter using transformer auxiliary winding. *IEEE Trans. Power Electron.* **2000**, *15*, 250–257. [[CrossRef](#)]
23. Gautam, D.S.; Musavi, F.; Eberle, W.; Dunford, W.G. A Zero-Voltage Switching Full-Bridge DC—DC Converter with Capacitive Output Filter for Plug-In Hybrid Electric Vehicle Battery Charging. *IEEE Trans. Power Electron.* **2013**, *28*, 5728–5735. [[CrossRef](#)]
24. Erickson, R.W.; Maksimović, D. *Fundamentals of Power Electronics*, 2nd ed.; Kluwer Academic: New York, NY, USA, 2001; ISBN 9780306480485.
25. Cremasco, A.; Rothmund, D.; Curti, M.; Lomonova, E.A. Voltage Distribution in the Windings of Medium-Frequency Transformers Operated with Wide Bandgap Devices. *IEEE J. Emerg. Sel. Top. Power Electron.* **2022**, *10*, 3587–3602. [[CrossRef](#)]
26. Liu, R.; Mi, C.C.; Gao, D.W. Modeling of Eddy-Current Loss of Electrical Machines and Transformers Operated by Pulsewidth-Modulated Inverters. *IEEE Trans. Magn.* **2008**, *44*, 2021–2028. [[CrossRef](#)]
27. Kazimierczuk, M.K. *High-Frequency Magnetic Components*, 2nd ed.; Wiley: Chichester, UK, 2014; ISBN 9781118717790.
28. Lidow, A.; de Rooij, M.; Strydom, J.; Reusch, D.; Glaser, J. *GaN Transistors for Efficient Power Conversion*, 3rd ed.; Wiley: Hoboken, NJ, USA, 2020; ISBN 9781119594376.